



Die Grenzen der  
Chemie neu ausloten?  
It takes  
#HumanChemistry

Wir suchen kreative Chemikerinnen und Chemiker,  
die mit uns gemeinsam neue Wege gehen wollen –  
mit Fachwissen, Unternehmertum und Kreativität für  
innovative Lösungen. Informieren Sie sich unter:

[evonik.de/karriere](https://evonik.de/karriere)

# A New Printable Alginate/Hyaluronic Acid/Gelatin Hydrogel Suitable for Biofabrication of In Vitro and In Vivo Metastatic Melanoma Models

Rafael Schmid, Sonja K. Schmidt, Rainer Detsch, Hannes Horder, Torsten Blunk, Stefan Schrüfer, Dirk W. Schubert, Lena Fischer, Ingo Thievensen, Stefanie Heltmann-Meyer, Dominik Steiner, Dominik Schneidereit, Oliver Friedrich, Anika Grüneboom, Hanna Amouei, Harald Wajant, Raymund E. Horch, Anja K. Bosserhoff, Andreas Arkudas, and Annika Kengelbach-Weigand\*

Two-dimensional (2D) cancer models have been the standard for drug development over the past few years, but they frequently do not resemble in vivo properties adequately. 3D models are superior in many aspects and are, therefore, more similar to human pathophysiology. Over the past years, the emerging field of biofabrication has made significant advances, resulting in even more sophisticated 3D models. With this study, a hydrogel is created for biofabrication that is suitable for mimicking the tumor microenvironment in vitro and is further tested as a new vascularized melanoma model in vivo. The alginate/hyaluronic acid/gelatin bioink shows good shape-fidelity, high cell survival rates, and enables successful cultivation of melanoma cells and adipose-derived stem cells as well as cell differentiation in vitro. In vivo, in the arteriovenous loop model, it proves to be a unique method to study melanoma progression, tumor vascularization, and ultimately and reliably metastases in an isolated and controlled environment. These results show that this 3D model is very application-oriented for molecular research and therapy development.

## 1. Introduction

Tissues and organs are complex, hierarchical structures that contain multiple cell types. Like most tissues, tumors, which have been described as complex “rogue”<sup>[1]</sup> organs by Balkwill et al., rely on vascularization and angiogenesis to guarantee the nutrient and oxygen supply of the surrounding cells. The resulting tumor microenvironment has been shown to play a crucial role in tumor promotion and in drug receptiveness.<sup>[2,3]</sup> Therefore, there is a need for complex models that mimic the microenvironment as accurately as possible.

This is why two-dimensional (2D) cell culture models are a rather good opportunity to get first insights into, e.g., how a

R. Schmid, S. Heltmann-Meyer, D. Steiner, R. E. Horch, A. Arkudas, A. Kengelbach-Weigand  
Laboratory for Tissue-Engineering and Regenerative Medicine  
Department of Plastic and Hand Surgery  
University Hospital of Erlangen  
Krankenhausstraße 12, 91054 Erlangen, Germany  
E-mail: annika.kengelbach-weigand@uk-erlangen.de  
S. K. Schmidt, A. K. Bosserhoff  
Institute of Biochemistry  
Friedrich-Alexander University of Erlangen-Nürnberg  
Fahrstraße 17, 91054 Erlangen, Germany  
R. Detsch  
Institute of Biomaterials  
Friedrich-Alexander University of Erlangen-Nürnberg  
Ulrich-Schalk-Straße 3, 91056 Erlangen, Germany

 The ORCID identification number(s) for the author(s) of this article can be found under <https://doi.org/10.1002/adfm.202107993>.

© 2021 The Authors. Advanced Functional Materials published by Wiley-VCH GmbH. This is an open access article under the terms of the Creative Commons Attribution-NonCommercial-NoDerivs License, which permits use and distribution in any medium, provided the original work is properly cited, the use is non-commercial and no modifications or adaptations are made.

DOI: 10.1002/adfm.202107993

H. Horder, T. Blunk  
Department of Trauma, Hand, Plastic and Reconstructive Surgery  
University of Würzburg  
Oberdürrbacher Straße 6, 97080 Würzburg, Germany  
S. Schrüfer, D. W. Schubert  
Institute of Polymer Materials  
Friedrich-Alexander University of Erlangen-Nürnberg  
Martensstraße 7, 91058 Erlangen, Germany  
L. Fischer, I. Thievensen  
Biophysics Group  
Department of Physics  
Friedrich-Alexander University of Erlangen-Nürnberg  
Henkestraße 91, 91052 Erlangen, Germany  
D. Schneidereit, O. Friedrich  
Institute of Medical Biotechnology  
Friedrich-Alexander University of Erlangen-Nürnberg  
Paul-Gordan-Straße 3, 91052 Erlangen, Germany  
A. Grüneboom  
Clinics of Internal Medicine III (Rheumatology and Immunology)  
University Hospitals Erlangen  
Friedrich-Alexander University Erlangen-Nürnberg  
Ulmenweg 18, 91054 Erlangen, Germany

therapeutic agent interacts with tumor cells, but the results are barely transferrable to the *in vivo* situation. Only a minority of agents showing good results in 2D cultures can be transferred to the clinics. This points out the need for more controllable and more physiological model systems mimicking the *in vivo* situation.

3D models, which are already found to deliver more transferrable results than 2D approaches, include the generation of cancer cell spheroids or organoid cultures. Models with single cells or spheroids encapsulated in different hydrogels, mimicking the extracellular matrix (ECM) of the tumor, are already in use either to examine the effects of certain therapeutics or to elucidate fundamental steps in cancer development and progression.

One possibility to improve the models further is the use of biofabrication. The research field of biofabrication is continuously growing with respect to tissue engineering and regenerative medicine.<sup>[4]</sup> One important branch of this research field deals with the 3D printing of functional tissues and organs for clinical, as well as for basic research applications.<sup>[5]</sup> Printable hydrogels with cells, the so-called bioinks, are used for creating the desired structures in a precise and controllable manner. The hydrogel should ideally resemble the natural ECM in terms of composition, structure and biomechanical properties. These properties vary from tissue to tissue, so they have to be tailored depending on the desired application.

There is a broad range of available hydrogels, either as single components adjustable by different concentrations or as blends with other hydrogels in order to obtain the desired properties, like ECM-similarity, printability, mechanical stability, and pore size. They range from originally animal-derived materials, like fibrin,<sup>[6]</sup> collagen,<sup>[7]</sup> gelatin,<sup>[8]</sup> and hyaluronic acid (HA),<sup>[9]</sup> to plant-derived materials, like alginate<sup>[10]</sup> and agarose,<sup>[11]</sup> and synthetic polymers like polyacrylamide. Some of these materials have to be functionalized to make them crosslinkable; collagen or gelatin form temperature-dependent hydrogels, while alginate forms non-covalent hydrogels with divalent ions. Naturally, some of these materials are biologically active and provide binding sites, others are inert for mammalian cells. One standard material is Matrigel, which is often used for cancer models, has a low shape-fidelity for bioprinting, lacks a defined composition, and further cannot be used in humans due to its origin. This illustrates the need for more defined and tunable bioinks that mimic the needed microenvironment. The use of an appropriate 3D matrix for a certain tissue or tumor type may improve the outcome of *in vitro* experiments, however, most of the standard models still lack the aspect of a defined vascularization.

The arteriovenous (AV) loop model has been proven to be a very effective option to vascularize a 3D scaffold in a controlled manner *in vivo*.<sup>[12]</sup> For this, a vascular loop is put into a chamber filled, e.g., with the desired hydrogel, which may also

contain cells. Long-term stability of the hydrogel guarantees that the loop stays in the initial position and enables blood flow through the construct. If a suitable hydrogel is used, angiogenesis can develop in the chamber over the course of a few weeks. The vessels sprout, pervading the hydrogel and guaranteeing supply of the cells incorporated in the hydrogel. Moreover, bioprintability of the hydrogel could help to increase controllability of the created model. This enables the distinct and precise deposition of cells in a desired arrangement within the chamber while the influence of different cell types and the vessels can be analyzed. Furthermore, stiffness or material gradients, porous structures, and functionalization can be better controlled.

Melanoma is a highly malignant skin cancer, originating from the pigment-producing melanocytes mainly in the basal cell layer of the epidermis or of hair follicles. It resembles an archetype of a malignant tumor whose development underlies endogenous factors, like skin type and genetic predisposition, as well as exogenous factors like UV-radiation. The course of the disease is characterized by early metastasis, already from small primary tumors. Metastases can be found not only in the skin but, e.g., also as nodal, lung, liver, brain, and bone metastases.<sup>[13]</sup> Novel drugs for more effective therapies also targeting advanced melanoma, where surgical resection is no longer possible, were developed and thus, the prognosis of melanoma patients has improved during the last decade. However, one prominent problem is the development of resistances against the applied therapeutics, leading to only temporary success. Therefore, there is still a huge demand for innovative models considering the tumor microenvironment, first to help elucidating unknown molecular processes in tumor development, progression, and ultimately metastases and, second, to find new therapeutics reliably targeting tumor cells and preventing the emergence of therapy resistance.

Here, we aimed to develop a versatile printable bioink that can be tuned in terms of stiffness and with the addition of tumor-associated cells, suitable to mimic the tumor microenvironment for *in vitro* as well in a new vascularized *in vivo* rat melanoma model, to be further used in research and drug development.

## 2. Results

### 2.1. Establishment of the Alg/HA/Gel Bioink

In this study, we developed a versatile three-component Alg/HA/Gel bioink (0.5% alginate, 0.1% HA, 3% gelatin) for different *in vitro* and *in vivo* applications. We focused on the selection of components based on the matrix composition of skin and on previous studies of different hydrogels for melanoma and breast cancer.<sup>[14]</sup>

To identify the ideal gelatin concentration for the Alg/HA/Gel bioink in terms of printability and cell survival, 3% to 6% gelatin were tested together with 0.5% alginate and 0.1% HA in beads (droplets generated using a pipette and a CaCl<sub>2</sub> bath) and printed in comparison (Figure 1a). The malignant melanoma cell line Mel 1m revealed growth of spherical colonies within one week in all different beads with no apparent microscopic differences between the conditions. In the printed constructs, we observed a significant decrease in surviving cells with

A. Grüneboom  
now ISAS e.V.  
Bioimaging  
Bunsen-Kirchhoff-Straße 11, 44139 Dortmund, Germany  
H. Amouei, H. Wajant  
Division Molecular Internal Medicine  
Department of Internal Medicine II  
University Hospital Würzburg  
Grombühlstraße 12, 97080 Würzburg, Germany

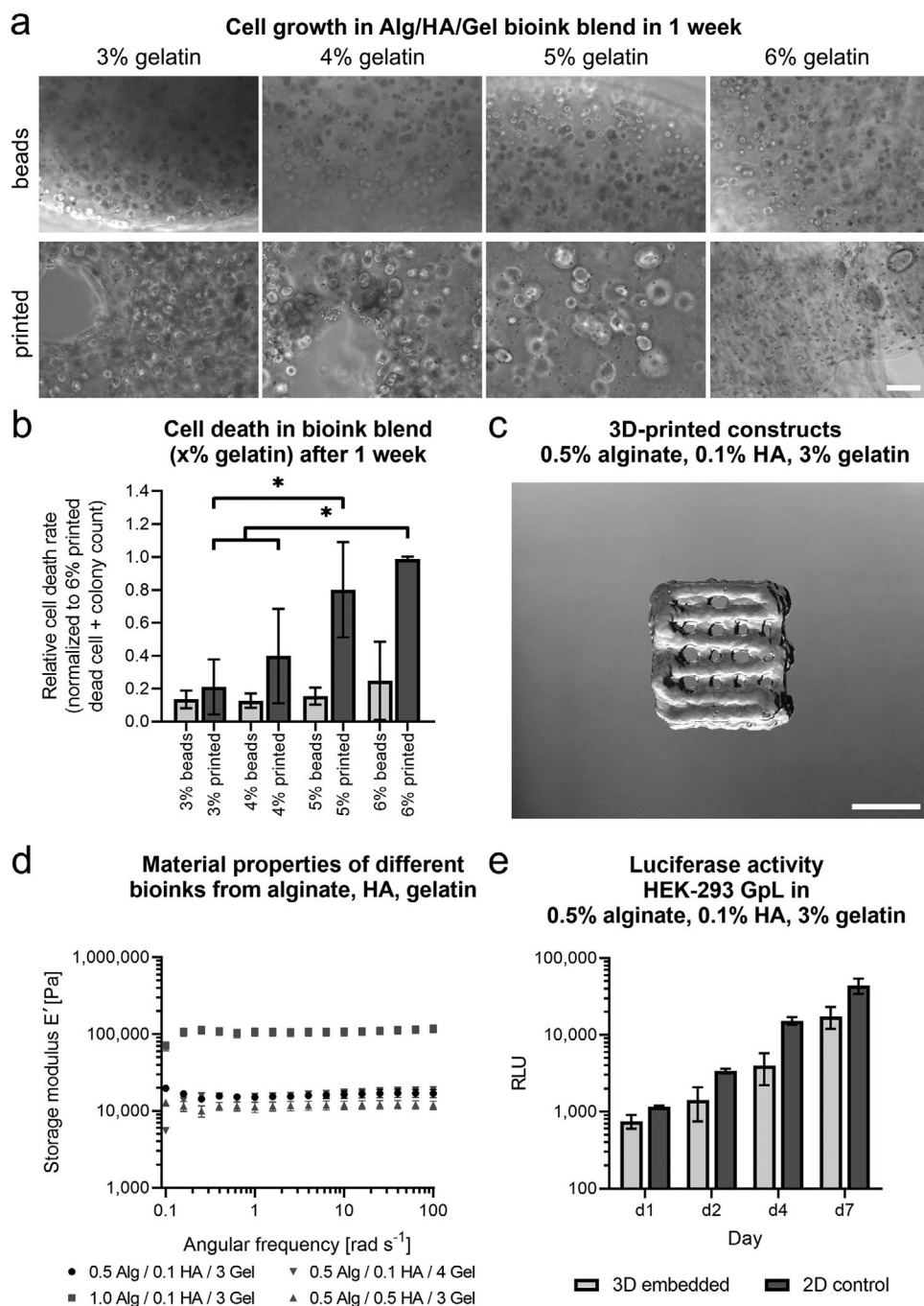


**Figure 1.** Establishment of a versatile Alg/HA/Gel (0.5% alginate, 0.1% HA, 3% gelatin) bioink; a) cell growth of Mel 1m in the bioink after one week comparing different gelatin concentrations printed or in beads (scale bar = 200  $\mu$ m); b) quantification of the cell death of Mel 1m in different gelatin concentrations, printed and in beads, data shown as mean  $\pm$  SD of biological replicates, \* $p \leq 0.05$  Kruskal–Wallis H test, Mann–Whitney U test, ( $n = 3$ ); c) macroscopic picture of a printed construct of the ink blend with 3% gelatin in three layers (scale bar = 5 mm); d) storage modulus  $E'$  of the ink blend and variations, data shown as mean  $\pm$  SD of technical replicates; e) luciferase activity of supernatants of HEK-293 cells expressing a GpL fusion protein grown in 3D in the bioink and conventional in 2D, data shown as mean  $\pm$  SD of technical replicates.

increasing gelatin concentration. This was quantified and set in relation to the presumed initial cell number (counted as the sum of colonies and dead cells of the printed group with 6% gelatin on day 7) (Figure 1b). Higher gelatin concentrations lead to a higher viscosity, which increases shear stress when maintaining the printing speed constant. When comparing the beads

with different gelatin concentrations, there was no significant difference. The best printing condition was 3% gelatin with almost 80% survival. Following experiments were performed with the concentrations: 0.5% alginate, 0.1% HA, 3% gelatin.

Extrusion-based 3D-printing (Figure 1c) of the Alg/HA/Gel bioink with a conical nozzle (580  $\mu$ m inner diameter) showed a

good printability with high shape-fidelity. The printed grid was clearly visible with its macroporous structure.

The Alg/HA/Gel bioink with 3% gelatin showed predominantly elastic properties in dynamic mechanical analysis (DMA) measurements (Figure 1d) as its storage modulus  $E'$  was much greater than the loss modulus  $E''$  ( $E' \gg E''$ , loss modulus not shown). The stiffness of the bioink was to a great extent tunable by increasing the alginate concentration to 1%. This resulted in an increase of the storage modulus from 15.5 kPa to 106.9 kPa at 1 rad  $s^{-1}$ . Increasing the HA content to 0.5% slightly reduced the stiffness of the hydrogel (11.3 kPa) while increasing the gelatin to 4% did not alter the stiffness range (15.1 kPa).

Production and release of large reporter proteins was used to see whether nutrient supply is secured and secreted factors can distribute through the Alg/HA/Gel bioink (Figure 1e). Embedded HEK-293 stably expressing a secreted fusion protein of TNFR2-Fc and the *Gaussia princeps* luciferase (TNFR2-Fc-GpL) showed an increase in the luciferase activity in the supernatant over seven days, demonstrating that diffusion of molecules smaller than 150 kDa is highly feasible.

## 2.2. Analysis of In Vitro Biocompatibility for Adipose-Derived Stem Cells

To further characterize the versatile applicability of this newly designed ink blend with the addition of stromal tumor-associated cells, we analyzed printing of immortalized adipose-derived mesenchymal stem cells (ADSCs) and their potential to differentiate in this bioink (Figure 2a). After 14 days, ADSCs showed small colony growth and good survival rates without spreading into the matrix.

ADSCs were differentiated into the adipogenic and the osteogenic lineage (Figure 2b). In standard 2D culture as well as embedded into the bioink in beads, ADSCs showed good differentiation potential into the adipogenic lineage. Using an Oil Red O staining, lipid vacuoles were clearly visible. The negative controls in standard medium remained undifferentiated. qPCR confirmed the significant adipogenic differentiation. Compared to the control, the expression of fatty acid binding protein 4 (FABP4) and lipoprotein lipase (LPL) increased after 21 days in differentiation medium.

Differentiation of ADSCs into the osteogenic lineage was proven with an alizarin red staining. In 2D, a strong red staining was observable. Stained microtome sections of the bioink beads showed a reddish color with darker red staining around colonies. Both negative controls (standard 2D and beads) in standard medium showed no staining. ADSCs showed a trend for a slightly increased expression of the osteogenic lineage marker alkaline phosphatase, biomineralization associated (ALPL) in the differentiated groups. These results reveal high biocompatibility not only with tumor cells but also normal cells while maintaining their differentiation potential.

## 2.3. Cell Cycle Analysis of Melanoma Cells within the Ink Blend

Printed Mel Im grew in larger colonies compared to ADSCs (Figure 3a). Interestingly, they showed no visible spreading or

migration within the matrix. The colonies reached diameters of more than 100  $\mu\text{m}$  after 14 days and often escaped the matrix.

To better define 3D cell proliferation, Mel Im transduced with the fluorescent ubiquitination-based cell cycle indicator (FUCCI) was both embedded into beads and printed with the bioink to analyze the influence of the printing process on the cell cycle (Figure 3b). Over one week, the single cells formed large colonies in all conditions. Here, quantification showed that there was no eminent difference in the cell cycle distribution between Mel Im FUCCI in standard 2D culture compared to cells within the ink blend printed or in beads on day 1 or day 7.

## 2.4. In Vivo AV Loop Implantation as a Versatile Melanoma Model

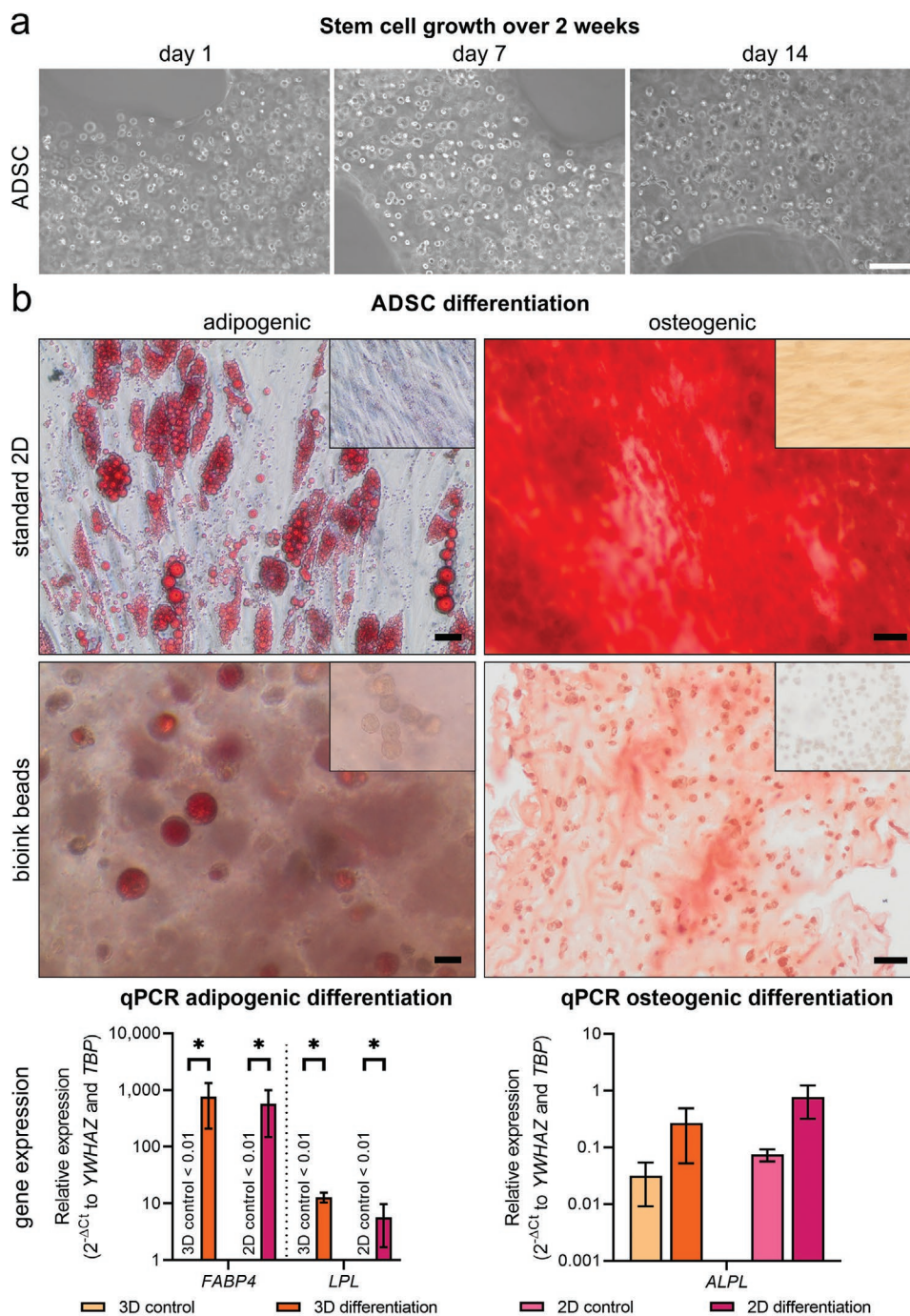
To add another component to the tumor microenvironment, vascularization was introduced. The hydrogel was evaluated in vascularized in vivo melanoma models using the rat AV loop model. Out of the 9 in vivo implantations, all of the animals survived and showed good wound healing with a typical phenotype. Implantation of Mel Im in the bioink over 4 weeks resulted in substantial tumor growth although the extent varied (Figure 4). In 7 out of the 9 animals, tumors grew out of the implantation chamber, in three animals this outgrown tumor was as big as the chamber itself.

Figure 4b shows the growth of two exemplary tumors within the chamber. HE, HMB-45, and Ki-67 stainings revealed highly proliferative melanomas in different sizes in the various explants. They were mainly clustered around the big loop vessels and expanded from there. The animal r1 (Figure 4b, left) showed AV loop vessel diameters of more than 500  $\mu\text{m}$ , while in the animal r8 (Figure 4b, right), with less than 100  $\mu\text{m}$  lumen diameter, the loop vessels were barely visible anymore due to the larger tumor mass. Depending on the size of the tumor, some remaining hydrogel can be detected. Hemorrhages can be seen in the HE sections and additionally also in optical sections (Figure 4c).

PET/CT scans after about 4 weeks also revealed a standardized uptake value (SUV) intense volume at the entrance of the implantation chambers (Figure 4b). For large outgrown tumors, this signal was also detectable outside the chamber.

Quantification of the tumor area in histological cross sections within the chamber is shown in Figure 4d. Quantified was the ratio of tumor tissue to the whole tissue excluding the remaining hydrogel. The mean tumor area ratio was 25.9% with the main tumor at the chamber entrance.

Whole-mount light microscopy and histology were used to image the explants. To visualize the vascularization, light sheet fluorescence microscopy and multiphoton microscopy were performed in combination with different stainings (Figure 5). During the clearing process, the use of bleach proved to be effective against hemorrhages (Figure 5a) which would otherwise absorb some of the light. The perfusion with FITC-BSA in agarose fills the lumen of the vessels, resulting in higher contrast to the tissue's autofluorescence. Within the chamber, the hydrogel itself was barely vascularized while tumorous tissue was well vascularized. Anti-CD31 staining revealed small capillaries, especially in the primary tumor tissue (Figure 5b). Notably, not all vessel structures were positive for



**Figure 2.** Stem cell cultivation within the ink blend; a) cell culture of printed ADSCs over two weeks (scale bar = 200  $\mu\text{m}$ ); b) ADSC differentiation in standard 2D as well as embedded in bioink beads, Oil Red O staining for adipogenic differentiation (scale bar = 20  $\mu\text{m}$ ), alizarin red staining for osteogenic differentiation (scale bar = 50  $\mu\text{m}$ ), controls in standard medium are shown in the smaller boxes; relative mRNA expression of different adipogenic and osteogenic markers, data shown as mean  $\pm$  SD of biological replicates,  $*p \leq 0.05$  Kruskal–Wallis H test, Mann–Whitney U test, ( $n = 3$ ).

CD31. The use of PAS histology revealed the smallest capillaries within the tumor mass. PAS-positive networks were detectable within the tumor mass, an indicator for vascular mimicry of melanoma cells. Areas with insufficient nutrient support already revealed necrosis (Figure 5c). These areas did not show an increased expression of the hypoxia-inducible factor 1-alpha (HIF1A) (not shown). Surrounding the tumor

mass, vimentin-positive mesenchymal cells were present. Further, CD68-positive macrophages were present in and surrounding the tumor mass. HMB-45 histology showed the typical morphology of a primary melanoma tumor mass. Collectively migrating clusters of melanoma cells were detectable within the surrounding tissue (Figure 5d). HMB-45-positive cells showed intravasation.

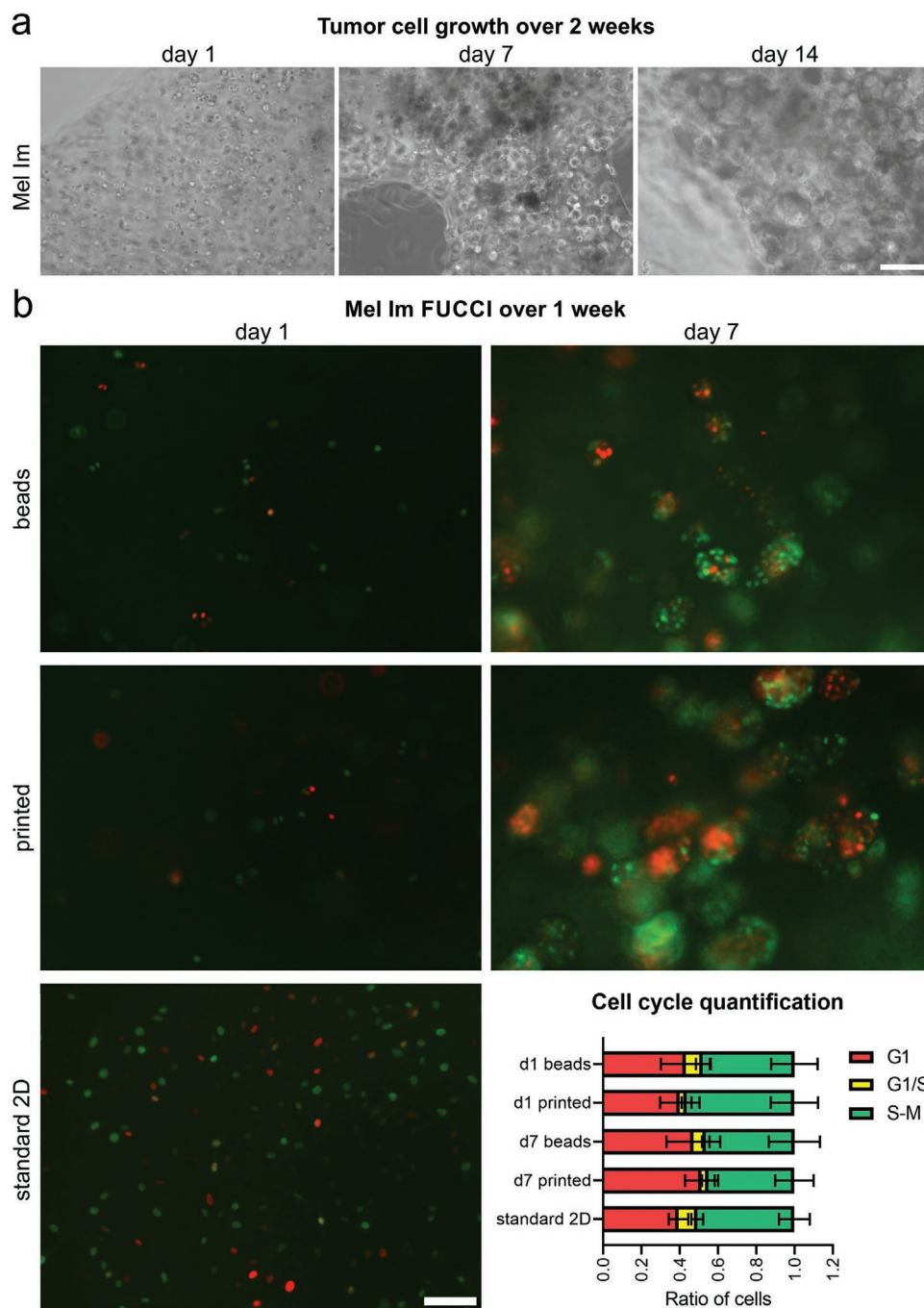


**Figure 3.** Malignant melanoma cell cultivation within the ink blend; a) Mel Im cell growth over two weeks (scale bar = 200  $\mu\text{m}$ ); b) cell cycle analysis of Mel Im FUCCI in beads, printed and 2D (scale bar = 100  $\mu\text{m}$ ), quantification data shown as mean  $\pm$  SD of 4 images of technical replicates.

To evaluate the tumor growth and metastatic behavior of Mel Im in the in vivo model, blood was taken once per week ( $n = 7$ ) to perform a MIA ELISA. This revealed a substantial increase in MIA in three of the animals, r1, r4, and r6, over four weeks (Figure 6a). These were the three animals with the largest outgrown tumor tissue (r4 depicted in Figure 4a).

After explantation, the lungs of animals ( $n = 5$ ) were fixed and also stained for HMB-45 (Figure 6b,c). All of the explanted lungs showed individual HMB45-positive cells or clusters, the start of proliferating metastases in the lungs. We quantified the

number of metastatic clusters per  $\text{mm}^2$ . The animal r4, which had the highest number of metastases, was also the one with the highest MIA serum levels.

### 3. Discussion

With this study, we evaluated the functionality of a newly developed Alg/HA/Gel bioink consisting of 3% gelatin, 0.5% alginate, and 0.1% HA. We defined its suitability for use as a basis for

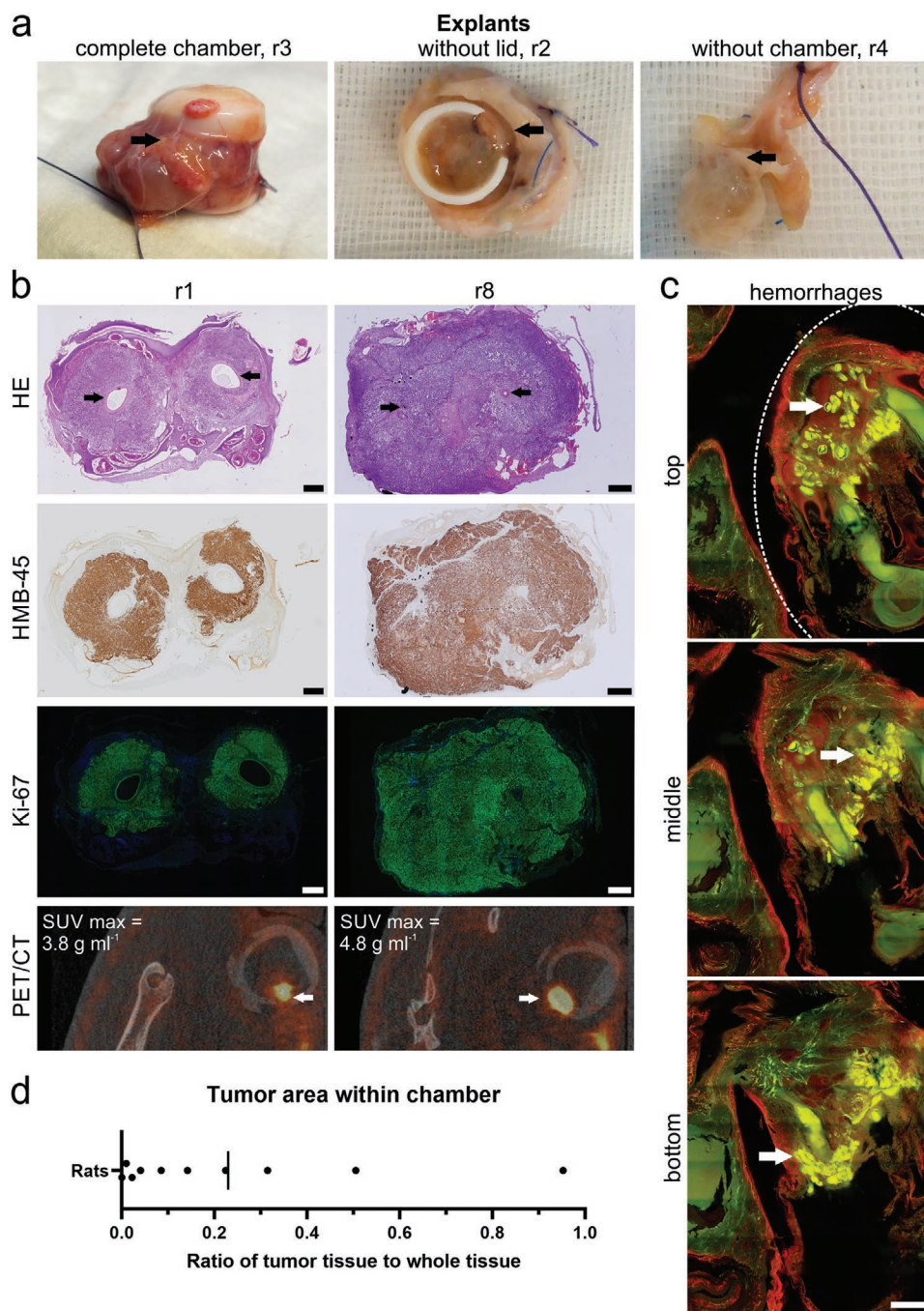


**Figure 4.** Explants of the in vivo tumor model; a) explant variation with and without the chamber, black arrows indicate the implantation chamber's entrance; b) the growth of two exemplary tumors within the chamber; HE, HMB-45, and Ki-67 staining of tumor sections, black arrows indicate the AV loop vessels, (scale bar = 500  $\mu$ m), PET/CT of the chamber after about 4 weeks (white arrows indicate the maximum SUV signal at the chamber's entrance); c) optical sections of different planes of one explant: FITC and autofluorescence (green) and ACTA2 and autofluorescence (red); dashed ellipse indicates the chamber inside surrounded by outgrown tumor, arrows indicate exemplary hemorrhages in proximity to the large AV loop vessels (scale bar = 1 mm); d) quantification of the tumor area ratio of histological sections within the chamber shown as dot plot with mean of  $\geq 2$  sections per animal.

biofabricated in vitro and in vivo melanoma models. As the tumor microenvironment not only consists of the tumor cells themselves, but also surrounding stromal cell types, immune cells, and in later stages, also vasculature, the requirements for the model are diverse. Extrusion-based bioprinting has various advantages

over standard hydrogel models. It offers the option to spatially arrange combinations of gels and cells in different concentrations in sophisticated macroporous structures and architectures.

Bioinks are not seldom a very artificial system that bring the cells in contact with substances that they would never

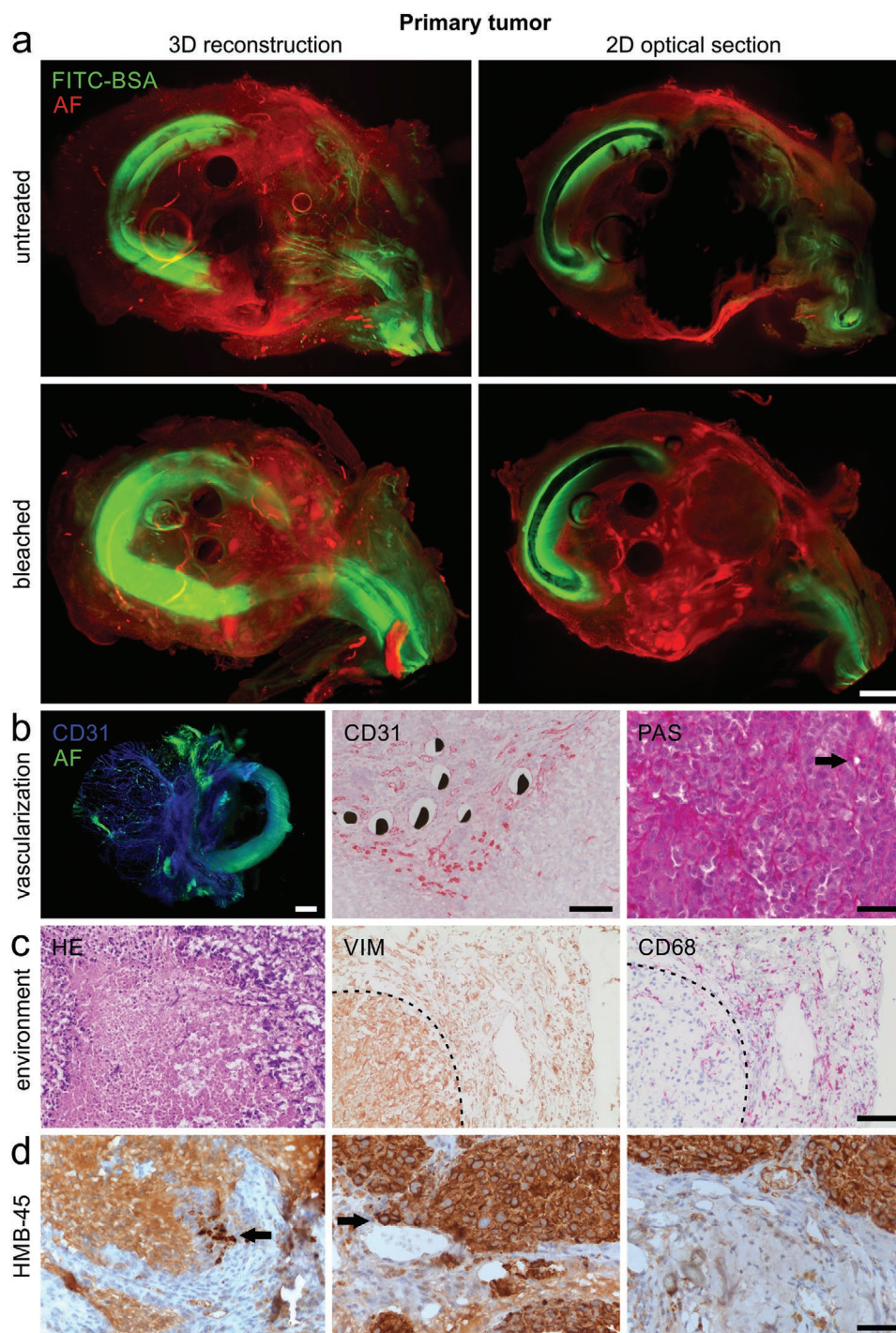


**Figure 5.** Visualization of the vascularization and tumor histology; a) the effect of bleaching on light microscopy (FITC-BSA perfusion in green, autofluorescence (AF) in red) of explanted melanoma samples (scale bar = 1 mm); b) vascularization, left: 3D reconstruction of an explant with CD31 (blue) staining with AF (green) (scale bar = 500  $\mu\text{m}$ ), middle: immunohistology for CD31 of the tumor (scale bar = 100  $\mu\text{m}$ ), right: histology PAS of the tumor (arrow indicates capillary, scale bar = 100  $\mu\text{m}$ ); c) environment in explants (dashed lines indicate tumor area), left: necrosis in tumor visualized via HE, middle: stromal cells positive for vimentin (VIM), macrophages positive for CD68 (scale bar = 100  $\mu\text{m}$ ); d) HMB-45, left: collective migration (arrow), middle and right: intravasation (arrows) (scale bar = 50  $\mu\text{m}$ ).

encounter in their normal in vivo environment. Many tumor models make use of Matrigel, a basement membrane mix of type IV collagen, laminin, entactin, heparan sulfate proteoglycans, and various growth factors, which is used as a gold

standard in several cases. It facilitates good tumor cell growth but has several disadvantages for biofabrication, like bad shape-fidelity,<sup>[15]</sup> the limited transferability and use in humans due to its mouse sarcoma origin, and batch-to-batch variations.

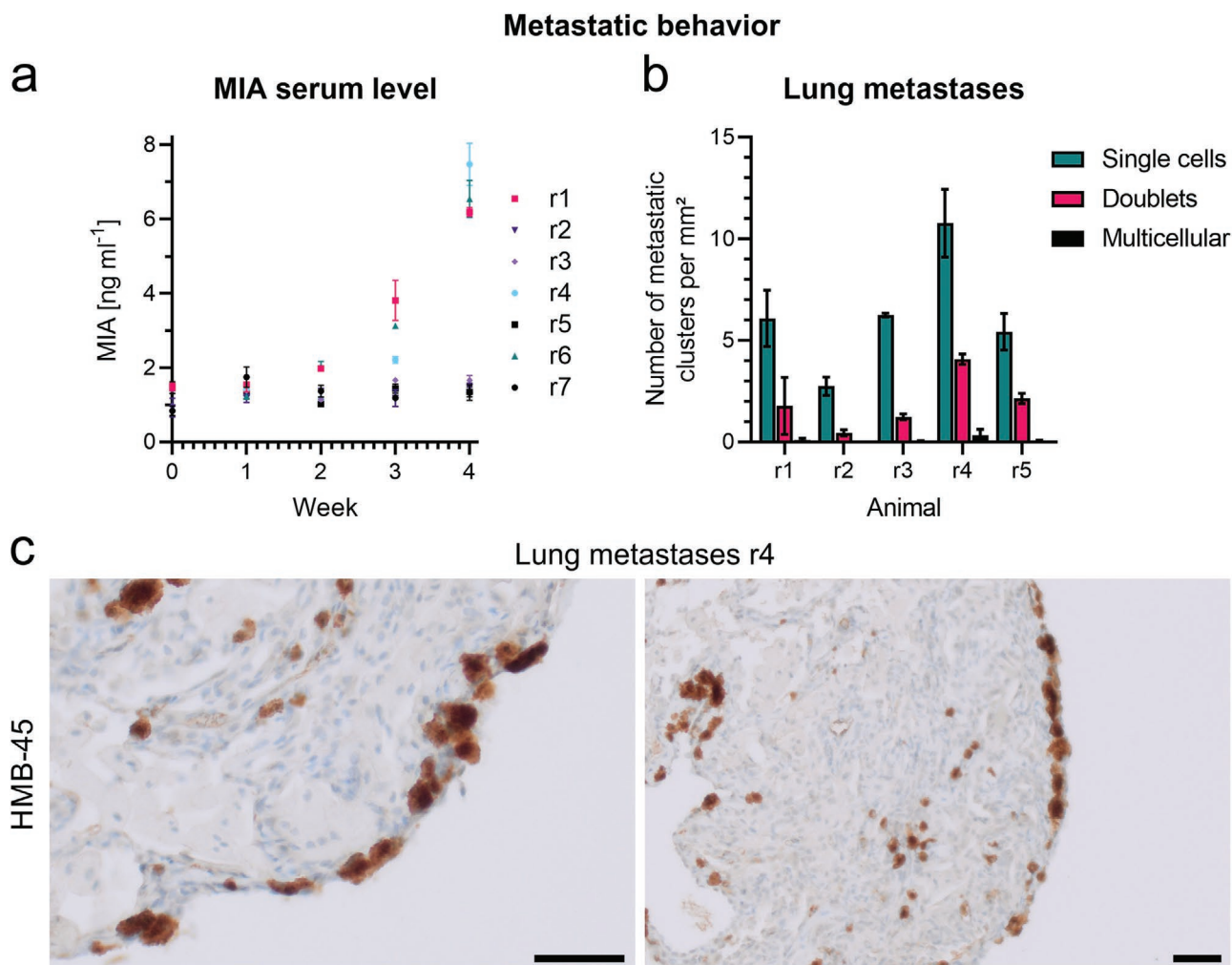


**Figure 6.** Metastases originating from the bioink implant in vivo; a) MIA serum levels of 7 rats measured over the in vivo implantation time, quantification data shown as mean  $\pm$  SD of 2 technical replicates; b) quantification of the lung metastases of 5 rats, shown as mean  $\pm$  SD of 2–3 histological sections per animal; c) histological sections of HMB-45-positive melanoma cells and clusters in the lung of the rat with the highest number of metastases (scale bar = 50  $\mu$ m).

Focusing on melanoma, we therefore included defined components that are found in skin or are originating from skin. We based the selection of components on previous studies, where we compared hydrogels from alginate, oxidized alginate bound to gelatin (ADA-GEL), and thiol-modified HA (HA-SH).<sup>[14]</sup> Bioinks with a selection of these components have been published in the past (e.g., alginate/HA,<sup>[16]</sup> alginate/gelatin<sup>[17]</sup>), but our current study shows the use of a combined bioink blend with proven use for bioprinted melanoma models. We created a bioink combining alginate, HA and gelatin, which are all known for their biocompatibility. One recent study made use of the components, however, in higher concentrations to create scaffolds, and without including cells into the ink.<sup>[18]</sup>

We used gelatin (3%) as hydrolyzed collagen and a high molecular weight HA (0.1%) as the basis for our bioink. Gelatin acts as a temperature-dependent thickener and enhances shape-fidelity substantially. With these two components, our bioink offers the possibility for integrin binding (gelatin) and CD44 interaction (HA). Besides skin hydration, HA plays

an important role in angiogenesis<sup>[19]</sup> as well as inflammatory response<sup>[20]</sup> and tissue repair.<sup>[21]</sup> Furthermore, it is part of the stem cell niche of and associated with drug resistance.<sup>[22]</sup> This indicates the importance of this glycosaminoglycan for the microenvironment and, consequently, for a model using this bioink. Notably, different molecular weights of HA can have a significant impact on cancer cell behavior and metastasis.<sup>[23]</sup> These properties could be used to further tailor the gel to specific needs. The printing evaluation of 2% alginate (PH 176) revealed good uniformity and accuracy of alginate constructs.<sup>[24]</sup> In the current work, alginate in a very low concentration (0.5%) was used as a crosslinkable component. As it is the only component of our bioink not present in skin, it was the main variable in the mixture. Although, alginate is not actively degradable by mammals, it has been successfully used in in vitro and in vivo models for many years.<sup>[25]</sup> Bioinks for extrusion-based bioprinting should have high shape-fidelity while also ensuring good cell survival. Ideally, the bioink is shear-thinning to reduce shear stress on cells. From our establishing experiments with

different gelatin concentrations (3-6%), it seems that more gelatin in the bioink greatly increases the shear forces during the printing process due to higher pressures needed for the same extrusion rate. These resulted in a significantly increased proportion of dead cells. With more gelatin, the viscosity and the gelation temperature of the bioink are increased,<sup>[8]</sup> resulting in significantly altered printing conditions. Although we tried to adjust pressure and temperatures for comparable shape-fidelity between the conditions, our results indicate that printing our Alg/HA/Gel ink blend with 3% gelatin is the most reliable option with the highest survival rates. Comparing this to the aforementioned publication of similar components with higher concentrations (4.5% alginate, 4.5% HA, 4.5% gelatin), we would not expect suitability as a bioink with cells due to the higher viscosity.<sup>[18]</sup> Thus, all the other experiments were performed with this ink blend that showed good shape-fidelity in our setup with a 580- $\mu\text{m}$  nozzle. The use of smaller nozzle diameters would decrease strand width and could be used for more filigree structures. The gel's stiffness proved to be tunable, another advantage over the standard Matrigel, opening up the usability for mimicking different niches. With a storage modulus  $E'$  of approx. 15.5 kPa at 1 rad  $\text{s}^{-1}$ , the Alg/HA/Gel is probably slightly softer than physiological skin; although Joodaki and Panzer<sup>[26]</sup> reviewed that skin has a Young's modulus of 1.1 kPa to 210 kPa in indentation studies. This is a very broad range that also covers our results. When the alginate content was increased to 1.0%, consequently resulting in an increase in crosslinking density, the stiffness increased almost sixfold. The effects of increasing the gelatin or HA were less pronounced as they are not active crosslinkers at 37 °C. Nevertheless, this could also alter cellular behavior within the gel. Tuning the stiffness of the bioink makes it also suitable to copy other microenvironments, e.g., the stiffness of trabecular bone is not reached (Young's modulus in the GPa range<sup>[27]</sup>). Here, metastatic cells would colonize the marrow cavity close to the stiff bone.<sup>[28]</sup> To ensure good diffusion properties through the hydrogel, we analyzed the production and release of a GpL fusion protein by HEK-293 transfectants cultured under 2D and 3D culture conditions. Here, we could prove that the fusion protein is increasingly released into the medium over time. With approx. 150 kDa as a dimer, its molecular weight is more than twice as high compared to the average eukaryotic protein.<sup>[29]</sup> Therefore, not only nutrients can diffuse into the hydrogel; also secreted substances can spread within the constructs and can diffuse out of it. This makes this hydrogel a valuable model to analyze the secreted factors in the tumor microenvironment. Additionally, targeted therapies with monoclonal antibodies can be evaluated.

To mimic the tumor microenvironment, we evaluated the use of the stromal ADSCs, one source of MSC. MSCs can be found in nearly all tissues and play an important (immunomodulatory) role in the tumor microenvironment by secreting various cytokines. They stimulate melanoma metastasis<sup>[30]</sup> and regulate extravasation.<sup>[31]</sup> Contrary to that, others have reported an inhibitory effect of ADSCs on melanoma growth.<sup>[32]</sup> This underlines the importance of defined 3D *in vitro* models for basic research combining ADSCs and melanoma cells to study their interaction. Over two weeks, those cells grew in small colonies within the printed matrix. It was possible to differentiate

the cells into the adipogenic and the osteogenic lineage. Therefore, this bioink enables researchers to include stem cells and mimic different niches within the body. While ADSCs grew in small colonies of few cells, over 14 days, Mel Im, especially those closer to the surface, grew in larger colonies that often were able to escape the hydrogel. This behavior is consistent with their tumor properties. Using the FUCCI construct,<sup>[33]</sup> cell cycle arrest can be visualized and quantified easily with a fluorescence microscope. The cells were able to proliferate without a cell cycle arrest over 7 days within the printed hydrogel.

The AV model is a versatile *in vivo* tool for tissue engineering research, for generating vascularized hard tissue (e.g., bone<sup>[34,35]</sup>) or soft tissue like lymphatic tissue.<sup>[36]</sup> A closed chamber, as we used for this study, promotes only intrinsic vascularization from the AV loop, and studying its interaction with hydrogels and cells becomes possible. This implicates that cells are only supplied via these vessels and in case of metastasis only can migrate via them. As always, *in vivo* models show variations between individuals, within the implantation chamber as well as outside of it. Typical standard melanoma models also show large variations between animals.<sup>[37]</sup> Additionally, the AV loop itself normally shows varying angiogenesis potential from animal to animal,<sup>[38,39]</sup> even without potential stimulating effects like melanoma cells. Our results are therefore in an expected range; we could not detect any unexpected problems caused by the bioink. In 7 out of 9 animals, the tumor proliferated out of the entrance of the implantation chamber clearly proving the feasibility of our new bioink as a valid model for tumor analysis enabling strong tumor proliferation. Once on the outside, further vascularization from the surrounding tissue is possible which further increases the growth rate. Inside the chamber, the dimensions are limited and upon implantation, an initially hypoxic environment is created.<sup>[40]</sup> In our histology, we could clearly see the typical size of the loop vessels. With increasing tumor size, vessels were almost collapsed due to the pressure built up by the proliferating tumor mass around it. Compression of intra-tumor vessels is typical for proliferating solid tumors.<sup>[41]</sup> A complete collapse would have resulted in starvation, hypoxia, and therefore, a higher degree of necrosis than we observed in the center of some tumors. Here, we could not detect a hypoxia-induced change in expression of HIF1A in tumor areas depending on the distance to the loop vessels (data not shown). This is in accordance with previous studies that reported a constitutive HIF1A expression for melanoma.<sup>[42]</sup> Also visible in histological and optical sections are masses of erythrocytes in the bioink, in and around the tumor. These hemorrhages are a clear indication for poorly organized and leaky networks of tumor-associated blood vessels caused by a high pro-angiogenic signaling within tumors (reviewed in detail by Schaaf et al.<sup>[43]</sup>). A further explanation could be vascular mimicry by melanoma cells,<sup>[44]</sup> which would also explain the CD31-negative vessel structures within the tumor. Hemorrhages are also a typical pathophysiological phenomenon found in brain metastases from melanoma.<sup>[45]</sup> A leaky vasculature opens an easy pathway for metastases. The intrinsic vascularization via the AV loop was visualized by whole-mount light microscopy, which has the advantage over conventional micro-CT<sup>[46]</sup> as soft tissues and hydrogels can also be visualized. After bleaching, which proved to be important for

our melanoma model with its hemorrhages, micro vessels were best observable using anti-CD31 antibodies. This revealed many capillaries within and around the tumor mass, as reported previously in other models.<sup>[47]</sup> Capillaries were correspondingly confirmed in anti-CD31 histology. Also, in PAS stainings, micro-capillaries were detectable within the tumors. Similar to previously reported histological analyses of primary malignant melanoma,<sup>[48]</sup> our PAS stainings of the primary tumors also revealed similar PAS-positive loops and networks. This is a further confirmation of the human-like pathophysiology of our model. The grown tumors show the typical histology of primary malignant melanomas, infiltration of cells into the surrounding tissue, and intravasation is also possible, resulting in metastases. In addition, the tumors were also surrounded and infiltrated by CD68-positive macrophages. These tumor-associated macrophages may also promote tumor growth and progression.<sup>[49]</sup> VIM-positive mesenchymal cells originating from the rat and surrounding the tumor are part of the tumor microenvironment and therefore also indicate the transferability of our model to the typical human pathophysiology.

The biggest primary tumors were also the ones that resulted in detectably increased MIA concentrations in the serum. MIA, which is produced by melanoma cells (and chondrocytes), is associated with tumor progression; later stages of the cancer lead to significantly elevated serum levels.<sup>[50]</sup> This makes it a valuable tool for diagnostics. The defined vascularization of the AV loop is a clear advantage over typical tumor models and especially metastases models (reviewed by Kuzo et al.<sup>[51]</sup> and Khanna and Hunt<sup>[52]</sup>) where cells are often injected into the bloodstream, skipping the invasion and intravasation. Here, especially the widely used B16 melanoma models should be mentioned that can be used as metastasis model for melanoma.<sup>[53]</sup> Intradermal injections would also mimic primary melanoma development but these experiments in mice have to be terminated early due to ulceration of the skin.<sup>[51]</sup> As it is a more complex model, Alg/HA/Gel in the AV loop is also more defined than typical subcutaneous tumor implantations, like xenograft models with human melanoma cells, as we are able to specifically design and mimic the desired microenvironment within the chamber. The possibility to use human melanoma cells instead of murine B16 cells makes the transfer of the results to the human pathophysiology more reliable. Our model further proved to be a consistent metastasis model with metastases found in all of the explanted lungs. They seemed to be arranged in mostly single cells or small clusters. An explanation for this could be that these cells are early metastatic cells that are still in a migratory phenotype (high BRN2 expression) and would have to switch to a proliferative phenotype (high MITF expression) first.<sup>[54]</sup>

Based on this analysis of the melanoma cells in Alg/HA/Gel in the AV loop, variations of the model, e.g., with the inclusion of ADSCs, differentiated cells or the use of other tumor entities, can be studied.

## 4. Conclusion

In conclusion, our new Alg/HA/Gel bioink is useful in various in vitro and in vivo tumor models. Not only does it provide

good shape-fidelity and high survival rates after extrusion-based printing, it is also a good tool to mimic the tumor microenvironment. In vivo, in combination with the AV loop, it is a unique model to study melanoma progression, vascularization, and ultimately metastases very similar to the pathophysiology in humans in an isolated and controlled environment. Therefore, this model will be a valuable tool for in detail analysis of molecular aspects of tumor progression and metastasis, in addition to drug development and testing.

## 5. Experimental Section

**Cell Culture:** The melanoma cell line Mel 1m, which is of metastatic origin, was cultivated in DMEM low glucose (Sigma-Aldrich, St. Louis, MO, USA) with L-glutamine (2 mM, Sigma-Aldrich, St. Louis, MO, USA), 10% FCS Superior (standardized fetal bovine serum, Biochrom GmbH, Berlin, Germany), and penicillin/streptomycin (100 U ml<sup>-1</sup>, 0.1 mg ml<sup>-1</sup>, Sigma-Aldrich). The immortalized ADSC line ASC/TERT1 (Evercyte GmbH, Vienna, Austria) was cultivated in EGM-2 (Lonza Group AG, Basel, Switzerland) with hydrocortisone, hFGF-B, VEGF, R3-IGF-1, ascorbic acid, hEGF, and heparin, and additionally supplemented with G418 (200 µg ml<sup>-1</sup>, Sigma-Aldrich) and 2% FCS Superior. TNFR2-Fc-GpL expressing HEK-293 transfectants were cultivated in RPMI-1640 with L-glutamine and sodium bicarbonate (Sigma-Aldrich) with 10% FCS Superior and penicillin/streptomycin. The incubator was set to 5% CO<sub>2</sub> at 37 °C. Medium was changed three times per week.

**Bioink Blends and Printing:** For the composition of a reproducible bioink, 0.5% m/v VIVAPHARM Alginate PH 176 (JRS PHARMA GmbH & Co. KG), 3–6% gelatin from porcine skin (gel strength ≈300 g Bloom, Type A, Sigma-Aldrich) during the establishment phase and 3% m/v during the main phase, and 0.1% m/v hyaluronic acid (1–2 MDa, CarboSynth Ltd, Compton, UK) were dissolved in PBS without Ca<sup>2+</sup> and Mg<sup>2+</sup> (Sigma-Aldrich) at 37 °C. A positive displacement pipette was used to resuspend 1 × 10<sup>6</sup> cells ml<sup>-1</sup> Mel 1m and either transfer the suspension into the 3 ml cartridges for printing or pipetting droplets directly into a CaCl<sub>2</sub> bath (10 min, 100 mM, Sigma-Aldrich), creating beads. In cartridges, the gel was cooled in a water bath at 15 °C for approximately 6–7 min (5–6 min for higher concentrations of gelatin) to gain a printable viscosity with shape-fidelity. Grids of 1 cm<sup>2</sup>, consisting of three layers with six strands each, were printed. The printing speed was 400 mm min<sup>-1</sup> with a conical needle (inner diameter 0.58 mm) and a pressure of 10–15 kPa using a Cellink Inkredible+ (Cellink, Boston, MA, USA) printer. After printing at room temperature, the constructs were crosslinked with CaCl<sub>2</sub> (100 mM) for 10 min, washed with medium, transferred into cell culture medium and incubated at 37 °C and 5% CO<sub>2</sub> for 14 days. Medium was changed three times per week.

For the evaluation of the cell survival after printing with different gelatin concentrations, microscopic images were evaluated after 1 week of incubation. The number of colonies and dead cells were summarized for the printed condition with 6% gelatin of each replicate and set as a reference for the presumed initial total cell number per image. The dead cells in all other conditions were counted and set in a ratio to the reference. Three images per condition and biological replicates ( $n = 3$ ) were evaluated.

**Luciferase Activity Assay:** We exemplarily used the TNFR2-Fc-GpL fusion protein of HEK-293 transfectants to measure the diffusion of large proteins. For the generation of HEK-293 cells stably expressing TNFR2-Fc-GpL, cells were transfected in confluent 15 cm tissue dishes in serum-free RPMI 1640 medium (15 ml). 2 ml RPMI 1640 were supplemented with a pCR3-based expression plasmid (12 µg) encoding Flag-tagged TNFR2-Fc-GpL. Polyethylenimine (PEI, 36 µl, 1 mg ml<sup>-1</sup>, Polyscience Inc., Warrington, PA, USA) was added dropwise with vortexing. After 15 min of incubation at RT, it was added to the culture dishes and incubated overnight. Then, the medium was changed to RPMI 1640 with 10% FCS and G418 (500 µg µl<sup>-1</sup>). The resulting clones were analyzed by measuring the GpL activity. The fusion protein is a dimer with approx. 150 kDa.

The stably transfected cells were encapsulated into the ink blend into beads with a concentration of  $1 \times 10^6$  cells  $\text{ml}^{-1}$ . The beads were weighed and an equal number of cells was seeded into a 24-well plate as 2D control. Both conditions were analyzed in triplicates with 1 ml medium. Luminescence measurements were performed on day 1, 2, 4, and 7. 2 hours prior to each measurement, the medium was changed. Afterwards, 11  $\mu\text{l}$  of the supernatant were diluted 1:10 in RPMI-1640 with 0.5% FCS Superior and 1% P/S, mixed and 50  $\mu\text{l}$  pipetted in duplicates into a black 96-well plate. Coelenterazine was dissolved in methanol (both Carl Roth GmbH & Co. KG, Karlsruhe, Germany) in a stock concentration of 2.45 mM and diluted to 1.5  $\mu\text{M}$  with PBS as a working solution. 25  $\mu\text{l}$  was added to each well and the relative luminescence units were measured immediately using a Centro LB 960 luminometer (Berthold Technologies GmbH & Co. KG, Bad Wildbad, Germany).

**DMA:** The elastic and viscous properties of the established bioink with 3% m/v gelatin, 0.5% m/v alginate and 0.1% m/v HA and its variations (varied to 1% m/v alginate, 4% m/v gelatin, or 0.5% m/v HA) were measured as previously described.<sup>[14]</sup> In short, films of 1 ml were prepared in a 12-well plate. They were crosslinked for 30 min in  $\text{CaCl}_2$  (100 mM). After overnight incubation at 37 °C in complete cell culture medium, the samples with a diameter of 18 mm were cut to 2 mm height. A DHR-3 rheometer (TA Instruments, New Castle, DE, USA) was equipped with a 20 mm plate-plate geometry and set to oscillating compression mode. An axial pre-force of 0.1 N was applied and the tests performed at 37 °C. A range from 0.1 to 100  $\text{rad s}^{-1}$  was covered. Average values and standard deviations were calculated from at least three measurements of technical replicates. Both moduli (storage modulus  $E'$  and loss modulus  $E''$ ) were determined.

**Differentiation Assays of ADSCs:** We used the ADSC cell line ASC/TERT1 to check whether differentiation into the adipogenic and the osteogenic lineage was possible within the ink blend.

Medium was changed three times per week. For the adipogenic differentiation, induction was done with IBMX (500  $\mu\text{M}$ , SERVA Electrophoresis GmbH, Heidelberg, Germany), insulin (1.7  $\mu\text{M}$ ), dexamethasone (1  $\mu\text{M}$ ), and indomethacin (200  $\mu\text{M}$ , all Sigma-Aldrich) in PBM-2 preadipocyte basal medium-2 (Lonza Group Ltd) with 10% FCS Superior and penicillin/streptomycin. Cells were embedded into the ink blend in a concentration of  $1 \times 10^7$  cells  $\text{ml}^{-1}$ . The induction was started immediately after the washing step. As a negative control, some of the beads were cultured in the standard culture medium. As a standard 2D control,  $2 \times 10^4$  cells  $\text{ml}^{-1}$  cells per well were seeded into 24-well plates, and the induction started 3–5 days after confluence. Again, differentiation media and standard culture medium were used as controls. After 21 days, the cultures were frozen for RNA isolation or stained with Oil Red O. Oil Red O (0.3 g, Sigma-Aldrich) were dissolved in isopropanol (100 ml, Carl Roth GmbH & Co. KG), filtered, and diluted with distilled water to 1.8 g  $\text{l}^{-1}$ . Samples were fixed with 10% formaldehyde for 30 min, washed with aqua dest. three times, incubated with 70% ethanol (Carl Roth GmbH & Co. KG) for 2 min, and incubated with the staining solution for 15 min. Samples were washed with distilled water and counter-stained with Mayer's hemalum (Merck KGaA, Darmstadt, Germany). The red staining was observed under an inverted microscope.

For the osteogenic differentiation, dexamethasone (0.1  $\mu\text{M}$ ), ascorbic acid (50  $\mu\text{M}$ ), and  $\beta$ -glycerophosphate (10 mM, all Sigma-Aldrich) were used in low-glucose DMEM with L-glutamine (Sigma-Aldrich) with 10% FCS Superior and penicillin/streptomycin. Cells were embedded into the ink blend in a concentration of  $2 \times 10^7$  cells  $\text{ml}^{-1}$  and differentiation induced directly after washing. Again, beads in standard culture medium were used as negative controls. The standard 2D control was seeded in 6-well plates ( $1 \times 10^5$  cells  $\text{ml}^{-1}$  cells per well) and differentiation was induced 3–5 days post confluence. After 21 days, some samples were frozen for RNA isolation and an alizarin red stain was performed. 2 g alizarin red S (AppliChem GmbH, Darmstadt, Germany) were dissolved in distilled water (100 ml) and its pH adjusted to 4.2 using 0.1% ammonium hydroxide (Thermo Fisher Scientific Inc., Waltham, MA, USA). Samples were fixed with 10% formaldehyde for 30 min and beads embedded into paraffin and cut using a microtome. Samples

**Table 1.** list of primers.

	Forward primer (5' → 3')	Reverse primer (5' → 3')
Human YWHAZ	ATGAGCTGGTTCAGAAGGCC	AAGATGACCTACGGGCTCTCT
Human TBP	TGCTGAGAAGAGTGTGCTGG	TGGCAGGCTGTTGTTCTGAT
Human LPL	ATGTGGTCCAGACGTCAACC	TCATGATGCAGGCCAATGGT
Human FABP4	ACTGCAGTCTCTCTCACC	CACCTTCTGGTGGCAAAGC
Human ALPL	CACGTCGATTGCATCTCTGG	GCCAGTACTTGGGGTCTTTC

were rehydrated where applicable and washed with distilled water and covered with the staining solution. After 30 min, samples were washed and observed under a microscope.

**RNA Isolation, cDNA Synthesis and qPCR:** RNA from 2D samples was isolated using the RNeasy Mini Kit with QIAshredders and an RNase-Free DNase Set (all QIAGEN GmbH, Hilden, Germany) according to the manufacturer's protocols. For the ink blend, a CTAB buffer was used, consisting of 2% CTAB, 2% PVP40, sodium chloride (1.4 M), Tris-HCl (100 mM, pH 8.0), and EDTA (20 mM, all Sigma-Aldrich). Immediately prior to the isolation, 1% 2-mercaptoethanol (Sigma-Aldrich) was added. The samples were vortexed with 600  $\mu\text{l}$  of the buffer 600  $\mu\text{l}$  chloroform (Sigma-Aldrich), mixed well and centrifuged at  $1.4 \times 10^4$  g for 2 min. The upper phase was taken, an equal volume of 70% ethanol (Sigma-Aldrich) added, and used with the RNeasy Mini Kit and the DNase. RNA concentrations were measured using a NanoDrop 2000c (Thermo Fisher Scientific Inc.). cDNA synthesis was performed using a QuantiTect Reverse Transcription Kit (QIAGEN GmbH). qPCR was performed using the SsoAdvanced Universal SYBR Green Supermix according to the manufacturer's protocols in a Bio-Rad CFX96 (all Bio-Rad Laboratories, Inc., Hercules, CA, USA) using the primers listed in **Table 1**. Evaluation was performed using the  $2^{-\Delta\Delta C_t}$  method with the housekeepers YWHAZ and TBP.

**Cell Cycle Analysis:** The fluorescent ubiquitination-based cell cycle indicator (FastFUCCI) construct makes it possible to visualize cell cycle progression.<sup>[33]</sup> Lenti-X 293T cells (Takara Bio Europe SAS, Saint-Germain-en-Laye, France) were transfected with pBOB-EF1-FAST-FUCCI-Puro (#86 849, Addgene, Watertown, MA, USA) and packaging plasmids (#8454, #12 260, Addgene) using Lipofectamine 2000 (Thermo Fisher Scientific Inc.). After 48 hours, the virus-containing supernatant was briefly centrifuged to pre-clean it and then concentrated (10  $\times$ ) using the LentiX-concentrator (Takara Bio Europe SAS). Mel 1m cells were seeded in a density of  $1 \times 10^5$  cells  $\text{ml}^{-1}$  cells per 9.6  $\text{cm}^2$  and after 24 h transduced with the concentrate. Successfully transduced stable cells were selected using puromycin (3.5  $\mu\text{g ml}^{-1}$ , Thermo Fisher Scientific Inc.).

These Mel 1m FUCCI cells were then further embedded or printed using the established bioink with 3% m/v gelatin as described above and cultivated for 14 days. Fluorescence images were taken on day 1, 7, and 14 on a fluorescence microscope (Olympus IX83, cellSens Software V1.16, Olympus Corporation, Tokyo, Japan) for the FUCCI's fluorescence proteins mAG and mKO2. The images were quantified manually by counting the cells in four representative pictures of technical replicates.

**In Vivo Implantation:** We used the AV loop model for implanting our hydrogels into male immune-deficient RNU rats (CrI:NIH-Foxn1<sup>tmw</sup>, Charles River Laboratories, Wilmington, MA, USA). The surgery was performed similar to earlier publications.<sup>[46]</sup> The experiments were approved by the Animal Care Committee of the University of Erlangen-Nürnberg (FAU) and the Government of Unterfranken, Germany (license number 55.2-2532-2-718). The animals were kept in individually ventilated cages in a standardized environment (light/dark cycles of 12 h, 20–22 °C, RH 46–48%).

The rats (body weight between 330 g and 440 g) were anesthetized using isoflurane (CP-Pharma, Burgdorf, Germany) and given medication intravenously (1 mg  $\text{kg}^{-1}$  meloxicam (Boehringer Ingelheim Vetmedica GmbH, Ingelheim am Rhein, Germany), butorphanol (1.5 mg  $\text{kg}^{-1}$ , CP-Pharma), enrofloxacin, (7.5 mg  $\text{kg}^{-1}$ , Bayer, Leverkusen, Germany). Anesthesia was monitored via pulse oximetry. The rats were placed on

their backs and their femoral vessels were dissected. A venous graft of the right femoral vein was harvested, flushed using an irrigation cannula with a heparin solution (50 IU ml<sup>-1</sup> (ratiopharm GmbH, Ulm, Germany), in isotone solution), and transferred to the left thigh. The distal end of the graft was connected (interrupted knots, 11-0 nylon sutures; Ethicon, Inc, Somerville, NJ, USA) to the femoral artery and the proximal end connected to the femoral vein via end-to-end anastomosis creating the AV loop. A PTFE chamber with an inner diameter of 10 mm and an inner height of 6 mm was used which was sutured onto the muscle with 6-0 sutures.

In 12-wells, 600 µl of the ink blend hydrogel were cast on top of filter papers soaked with 100 mM CaCl<sub>2</sub>. In each well, another soaked filter paper was put on top and 200 µl CaCl<sub>2</sub> (100 mM) pipetted onto it. After 10 min, a 10-mm punch was used to create two smaller disks. A 4 mm punch was used to create a smaller inner disk. One of the larger disks was put into the chamber, the loop placed onto it and the center filled with the small disk. The entrance was closed with an approx. 1% human fibrin clot (Baxter, Deerfield, IL, USA). 1 × 10<sup>6</sup> Mel 1m cells were resuspended in 300 µl of the hydrogel and cast directly onto the loop. CaCl<sub>2</sub> (100 mM) was used to crosslink the gel for 10 min. HBSS (Sigma-Aldrich) was used for washing. Afterwards, the last large disk was placed on top and the chamber closed with its lid.

The lid was sutured onto the chamber. Then, the wounds were closed with subcutaneous interrupted sutures (6-0 polypropylene sutures) and simple interrupted sutures (4-0 polypropylene sutures, both Ethicon, Inc). Enoxaparin sodium (10 mg kg<sup>-1</sup>, Sanofi S.A., Paris, France) was administered directly after the surgery and then two days postoperatively together with meloxicam (1 mg kg<sup>-1</sup>). Enrofloxacin was added to the drinking water for the first five days, additionally with meloxicam from day 3 to day 7. The chambers were explanted after 4 weeks.

**Measurement of the MIA Serum Concentrations:** As tumor marker, the human MIA level in the blood serum was measured. The rats were anesthetized once per week and blood taken through a lateral tail vein and collected using S-Monovette 1.1 ml Z-Gel tubes (SARSTEDT AG & Co. KG, Nümbrecht, Germany). After centrifugation, the serum was frozen and then used in duplicates for the MIA ELISA according to the manufacturer's protocol (Roche, Holding AG, Basel, Switzerland). The standard was evaluated with a four parameter rodbard function.

**PET/CT Imaging:** After about 4 weeks, the animals were imaged using positron emission tomography (PET) / computed tomography (CT) by the Preclinical Imaging Platform (PIPE) Erlangen as described previously.<sup>[55]</sup> In short, anesthetized rats were intravenously injected with 2-deoxy-2-[<sup>18</sup>F]fluoro-D-glucose (5.5 MBq). PET/CT was performed in a hybrid scanner (Inveon; Siemens, Munich, Germany). CT images were reconstructed using a Feldkamp algorithm and a Shepp-Logan filter and combined with the PET images (reconstruction with the system manufacturer's implementation of a 3D-ordered subsets expectation maximization and a shifted Poisson maximum a posteriori algorithm).

**Staining, Processing and Imaging of Vascularized Implants:** To visualize the vasculature, two methods were performed: a FITC-BSA-agarose perfusion of, or an injection with labeled anti-CD31 antibodies into anesthetized (isoflurane) and analgized (butorphanol) rats.

For the FITC-BSA staining, the rats were perfused with a heparin-containing (100 IE ml<sup>-1</sup>), isotonic saline solution via cannulation of the aorta followed by perfusion with albumin-fluorescein isothiocyanate conjugate (5 mg ml<sup>-1</sup>, 10 ml, Sigma) solved in 1% m/v ultralow-melting SeaPrep agarose (Lonza Group AG). Immediately after perfusion, rats were transferred into an ice bath to induce hardening of the agarose-filled vasculature.

Alternatively, the rats were injected intravenously with anti-CD31 antibodies (1 ml, 0.05 mg ml<sup>-1</sup>, labeled with Alexa Fluor 647, Clone TLD-3A12, MCA1334A647, Bio-Rad Laboratories, Inc.). After 20 min, the rats were sacrificed. The supplying vessels of the chamber were ligated and the chamber and the possibly outgrown tumor explanted.

The explants were fixed with 4% formaldehyde (Carl Roth GmbH & Co. KG) for 8–12 h at 4–8 °C. Bleaching was performed using 1.75% H<sub>2</sub>O<sub>2</sub> (Carl Roth GmbH) and 5% DMSO (Sigma-Aldrich) in PBS. Samples were incubated in the bleaching buffer for 4 h at 4–8 °C. For the ACTA2

staining, the explants were blocked (5% DMSO, 0.1% Tween 20, 1% BSA, 5 mM EDTA in PBS, all Sigma-Aldrich) for five days at 4–8 °C. This was followed by an antibody labeling with anti-ACTA2 antibody (1:200 in blocking buffer, clone 1A4, MSK 030-05, Zytomed Systems GmbH, Bargteheide, Germany), two washing steps (5% DMSO, 0.1% Tween 20 in PBS) for one day each and secondary labeling with goat anti-Mouse IgG (H+L, Alexa Fluor Plus 647, A32728, Thermo Fisher Scientific Inc.) 1:500 in blocking buffer for five days and two additional washing steps.

Afterwards, tissue optical clearing was performed as described previously.<sup>[47,56]</sup> In detail, the fixed tissue was dehydrated by an increasing series of ethanol solutions: samples were incubated in 50%, 70%, and two times in 100% ethanol for 4–24 h at 4–8 °C in slightly shaking tubes. After tissue dehydration, samples were transferred to ethyl cinnamate (Sigma Aldrich) and cleared for at least 4 h at room temperature. The cleared explants were imaged using light sheet fluorescence microscopy (LSFM) or multiphoton microscopy.

LSFM of optically cleared arteriovenous loops was performed with an Ultramicroscope II (LaVision BioTec GmbH, Bielefeld, Germany) including an Olympus MVX10 zoom body, a LaVision BioTec Laser Module, and an Andor Neo sCMOS Camera with a pixel size of 6.5 µm, and 2x detection optics with a numerical aperture (NA) of 0.5. The optical zoom was adjusted to 0.8x, 1x, or 2x and the light sheet thickness was set in a range of 4 µm to 10 µm.

Visualization of FITC-BSA labelled agarose filled vasculature was conducted via a 488-nm optically pumped semiconductor laser (OPSL) with detection filters at 525/50 nm. General tissue autofluorescence was excited at 561 nm via an optically pumped OPSL and emitted signals were detected at 620/60 nm. A 647 nm diode laser was used with the filter 680/30 nm was used for CD31-AF647. Generated data were collected with ImspectorPro software version 5.1.304 and processed with Imaris software version 9.1 (Bitplane AG, Zürich, Switzerland).

Two-photon microscopy was performed using a multiphoton microscope (TriMScope II, LaVision BioTec). Microscope specifications as well as image analysis capability of ultrastructural myofibrillar architectures were described previously.<sup>[57]</sup> Signals were generated using a mode-locked ps-pulsed Ti:Sa laser (Chameleon Vision II, Coherent, Santa Clara, USA) at an 810 nm wavelength. The two-photon excited fluorescence was recorded using a 525/50 nm band-pass (Chroma Technology group, Acal BFi Germany GmbH, Dietzenbach, Germany) filter for green-spectrum FITC detection and a 675/60 nm band-pass filter (Chroma Technology group) for red-spectrum autofluorescence detection in conjunction with a non-descanned photomultiplier tube (PMT) (H 7422–40 LV 5M, Hamamatsu Photonics, Hamamatsu City, Japan) in backscattered configuration. A 10 × plan fluor (Nikon Corporation, Minato, Japan) objective was used on the excitation side of the setup. The recorded images had a voxel size of 4 × 4 × 7 µm<sup>3</sup> in images with a 1 × 10<sup>3</sup> µm<sup>2</sup> field of view. The Images were recorded as 3D mosaics and later stitched and 3D reconstructed using ImageJ.<sup>[58]</sup>

**Histology:** After light microscopy, the constructs were embedded into paraffin and 5 µm histological sections cut using a microtome (Leica Microsystems, Wetzlar, Germany). Several histological HE and PAS (Leica Autostainer XL, Leica Microsystems), and HMB-45 (ENZ-C34930, Enzo Life Sciences, Inc., Farmingdale, NY, USA; VENTANA BenchMark ULTRA, Roche) stainings were done by the local pathological institute (University Hospital Erlangen). HMB-45 stainings of sections of chambers were quantified semi-automatically using the LAS (version 4.12.0), and the tumor area was set in relation to the total tissue area without the remaining hydrogel (measured manually in adjacent HE stainings *n* = 9). Per animal, at least two sections of the chamber were quantified and the means of the tumor ratio calculated. For the metastases in the lungs, ImageJ was used to manually count the metastatic cells and clusters, and to measure the area of the lungs (2–3 sections per animal, *n* = 5).

A Ki-67 antibody (1:200, clone SP6, RBK027-05, Zytomed Systems GmbH) was used to visualize proliferative cells. A citrate buffer pH 6 (Dako Target Retrieval, Agilent, Santa Clara, CA, USA) was used for antigen retrieval. For staining, the CSA II Biotin-Free Tyramide Signal Amplification System (Dako, Agilent, Santa Clara, CA, USA) was used

according to the manufacturer's instructions. Counterstaining was performed with DAPI (1 µg ml<sup>-1</sup>, Thermo Fisher Scientific Inc.).

Histology for the vascularization used antibodies against CD31 (1:70, 503-11114, Zytomed Systems GmbH, pretreatment with citrate buffer pH 6). The detection system was a polymer kit (ZytoChem Plus AP, all Zytomed Systems GmbH). Sections were counter-stained with Mayer's hemalum.

Hypoxia was detected using antibodies against HIF1A (1:100, clone H1alpha67, NB100-123, Novus Biologicals, Bio-Techne GmbH, Wiesbaden Nordenstadt, Germany, pretreatment with citrate buffer pH 6). The detection system was a peroxidase/DAB kit (DAKO EnVision, Agilent).

The microenvironment was visualized using antibodies against vimentin and CD68. For the anti-vimentin staining (1:150, clone V9, MSK023, Zytomed Systems GmbH, pretreatment with citrate buffer pH 6), the EnVision system was used. For the anti-CD68 staining (1:300, clone ED1, MCA341R, Bio-Rad, pretreatment with pronase (Sigma-Aldrich)), the polymer kit was used.

**Statistics and Figures:** During the establishing phase of the gelatin concentrations, the experiments were performed three times ( $n = 3$ ). Subsequent in vitro experiments were performed once ( $n = 1$ ) to prove feasibility but the differentiation assay was also performed three times ( $n = 3$ ). In vivo, 9 animals were used for the implantation of the Alg/HA/Gel hydrogel.

Statistical analysis was performed by using IBM SPSS statistics software V24 (SPSS Software/IBM, Armonk, NY, USA). Differences between groups were analyzed using the Kruskal–Wallis H test, followed by a Mann–Whitney U test for post hoc analysis; the asymptotic significance was used. Significant p-value was set to  $\leq 0.05$ . Figure 4 shows a dot plot with mean and Figures 1, 2, 3, and 6 means  $\pm$  standard deviations and were created with GraphPad Prism 8.1.2 (GraphPad Software, La Jolla, CA, USA). Depicted microscopic images were arranged and edited with CorelDRAW X6 and Corel PHOTO-PAINT X6 (Corel Corporation, Ottawa, ON, Canada) and the contrast of the FUCI images was enhanced with Adobe Photoshop 19.1.8 (Adobe Inc., Mountain View, CA, USA).

## Acknowledgements

A.K.B., A.A., and A.K.-W. contributed equally to this work. The authors would like to thank Stefan Fleischer, Ilse Arnold-Herberth, and Evelyn Maurer for their excellent technical support. The authors would also like to thank Jonas Hazur and Aldo R. Boccaccini for their scientific support. Anja K. Bosserhoff, Andreas Arkudas, and Annika Kengelbach-Weigand contributed equally to this work. The work was funded by the Deutsche Forschungsgemeinschaft (DFG, German Research Foundation), Project number 326998133, TRR 225 (subprojects C03 and A01, A07, B06, B08, C02, C04).

Open access funding enabled and organized by Projekt DEAL.

## Conflict of Interest

The authors declare no conflict of interest.

## Data Availability Statement

Data available on request from the authors.

## Keywords

bioinks, metastasis, stem cells, tissue engineering, tumors

Received: August 11, 2021

Revised: September 27, 2021

Published online: October 13, 2021

- [1] F. R. Balkwill, M. Capasso, T. Hagemann, *J. Cell Sci.* **2012**, *125*, 5591.
- [2] E. Hirata, E. Sahai, *Cold Spring Harbor Perspect. Med.* **2017**, *7*, a026781.
- [3] N. Nagarsheth, M. S. Wicha, W. Zou, *Nat. Rev. Immunol.* **2017**, *17*, 559.
- [4] T. Ramos, L. Moroni, *Tissue Eng., Part C* **2020**, *26*, 91.
- [5] J. Groll, T. Boland, T. Blunk, J. A. Burdick, D. W. Cho, P. D. Dalton, B. Derby, G. Forgacs, Q. Li, V. A. Mironov, L. Moroni, M. Nakamura, W. Shu, S. Takeuchi, G. Vozzi, T. B. Woodfield, T. Xu, J. J. Yoo, J. Malda, *Biofabrication* **2016**, *8*, 013001.
- [6] S. England, A. Rajaram, D. J. Schreyer, X. Chen, *Bioprinting* **2017**, *5*, 1.
- [7] A. Lee, A. R. Hudson, D. J. Shiwardski, J. W. Tashman, T. J. Hinton, S. Yermeni, J. M. Bliley, P. G. Campbell, A. W. Feinberg, *Science* **2019**, *365*, 482.
- [8] L. Ouyang, R. Yao, Y. Zhao, W. Sun, *Biofabrication* **2016**, *8*, 035020.
- [9] J. Hauptstein, T. Bock, M. Bartolf-Kopp, L. Forster, P. Stahlhut, A. Nadernezhad, G. Blahetek, A. Zerneck-Madsen, R. Detsch, T. Jungst, J. Groll, J. Tessmar, T. Blunk, *Adv. Healthcare Mater.* **2020**, *9*, 2000737.
- [10] J. Hazur, R. Detsch, E. Karakaya, J. Kaschta, J. Tessmar, D. Schneiderreit, O. Friedrich, D. W. Schubert, A. R. Boccaccini, *Biofabrication* **2020**, *12*, 045004.
- [11] D. F. Duarte Campos, A. Blaesus, M. Weber, J. Jakel, S. Neuss, W. Jahn-Dechent, H. Fischer, *Biofabrication* **2013**, *5*, 015003.
- [12] A. Weigand, R. E. Horch, A. M. Boos, J. P. Beier, A. Arkudas, *Eur. Surg. Res.* **2018**, *59*, 286.
- [13] F. Tas, *J. Oncol.* **2012**, *2012*, 647684.
- [14] R. Schmid, S. K. Schmidt, J. Hazur, R. Detsch, E. Maurer, A. R. Boccaccini, J. Hauptstein, J. Tessmar, T. Blunk, S. Schrufer, D. W. Schubert, R. E. Horch, A. K. Bosserhoff, A. Arkudas, A. Kengelbach-Weigand, *Cancers* **2020**, *12*, 2320.
- [15] S. K. Schmidt, R. Schmid, A. Arkudas, A. Kengelbach-Weigand, A. K. Bosserhoff, *Cells* **2019**, *8*.
- [16] C. Antich, J. de Vicente, G. Jimenez, C. Chocarro, E. Carrillo, E. Montanez, P. Galvez-Martin, J. A. Marchal, *Acta Biomater.* **2020**, *106*, 114.
- [17] B. Yao, T. Hu, X. Cui, W. Song, X. Fu, S. Huang, *Biofabrication* **2019**, *11*, 045020.
- [18] M. Bertuola, B. Araújo, U. Gilibert, A. Gonzalez-Wusener, M. Pérez-Recalde, C. O. Arregui, É. B. Hermida, *J. Mater. Sci.* **2021**, *56*, 15327.
- [19] M. Slevin, J. Krupinski, J. Gaffney, S. Matou, D. West, H. Delisser, R. C. Savani, S. Kumar, *Matrix Biol.* **2007**, *26*, 58.
- [20] J. Lesley, R. Hyman, N. English, J. B. Catterall, G. A. Turner, *Glycoconjugate J.* **1997**, *14*, 611.
- [21] D. Jiang, J. Liang, P. W. Noble, *Annu. Rev. Cell Dev. Biol.* **2007**, *23*, 435.
- [22] M. A. Solis, Y. H. Chen, T. Y. Wong, V. Z. Bittencourt, Y. C. Lin, L. L. Huang, *Biochem. Res. Int.* **2012**, *2012*, 346972.
- [23] Z. K. Price, N. A. Lokman, C. Ricciardelli, *Cancers* **2018**, *10*.
- [24] E. Karakaya, L. Fischer, J. Hazur, A. R. Boccaccini, I. Thievensen, R. Detsch, *Trans. Addit. Manuf. Meets Med.* **2020**, *2*.
- [25] U. Rottensteiner, B. Sarker, D. Heusinger, D. Dafinova, S. N. Rath, J. P. Beier, U. Kneser, R. E. Horch, R. Detsch, A. R. Boccaccini, A. Arkudas, *Materials* **2014**, *7*, 1957.
- [26] H. Joodaki, M. B. Panzer, *Proc. Inst. Mech. Eng., Part H* **2018**, *232*, 323.
- [27] D. Wu, P. Isaksson, S. J. Ferguson, C. Persson, *Acta Biomater.* **2018**, *78*, 1.
- [28] J. A. Sterling, J. R. Edwards, T. J. Martin, G. R. Mundy, *Bone* **2011**, *48*, 6.
- [29] L. P. Kozłowski, *Nucleic Acids Res.* **2017**, *45*, D1112.
- [30] W. Zhu, W. Xu, R. Jiang, H. Qian, M. Chen, J. Hu, W. Cao, C. Han, Y. Chen, *Exp. Mol. Pathol.* **2006**, *80*, 267.
- [31] D. Correa, R. A. Somoza, P. Lin, W. P. Schiemann, A. I. Caplan, *Int. J. Cancer* **2016**, *138*, 417.

- [32] J. O. Ahn, Y. R. Coh, H. W. Lee, I. S. Shin, S. K. Kang, H. Y. Youn, *Anticancer Res.* **2015**, 35, 159.
- [33] S. B. Koh, P. Mascalchi, E. Rodriguez, Y. Lin, D. I. Jodrell, F. M. Richards, S. K. Lyons, *J. Cell Sci.* **2017**, 130, 512.
- [34] S. Winkler, H. Mutschall, J. Biggemann, T. Fey, P. Greil, C. Korner, V. Weisbach, A. Meyer-Lindenberg, A. Arkudas, R. E. Horch, D. Steiner, *Tissue Eng., Part A* **2020**.
- [35] A. M. Boos, J. S. Loew, A. Weigand, G. Deschler, D. Klumpp, A. Arkudas, O. Bleiziffer, H. Gulle, U. Kneser, R. E. Horch, J. P. Beier, *J. Tissue Eng. Regener. Med.* **2013**, 7, 654.
- [36] J. W. Robering, M. Al-Abboodi, A. Titzmann, I. Horn, J. P. Beier, R. E. Horch, A. Kengelbach-Weigand, A. M. Boos, *Tissue Eng., Part A* **2020**.
- [37] C. W. Stackpole, *Nature* **1981**, 289, 798.
- [38] A. Arkudas, G. Prymachuk, T. Hoereth, J. P. Beier, E. Polykandriotis, O. Bleiziffer, R. E. Horch, U. Kneser, *Tissue Eng., Part A* **2009**, 15, 2501.
- [39] A. Arkudas, J. Tjiawi, O. Bleiziffer, L. Grabinger, E. Polykandriotis, J. P. Beier, M. Sturzl, R. E. Horch, U. Kneser, *Mol. Med.* **2007**, 13, 480.
- [40] Q. Yuan, O. Bleiziffer, A. M. Boos, J. Sun, A. Brandl, J. P. Beier, A. Arkudas, M. Schmitz, U. Kneser, R. E. Horch, *BMC Biotechnol.* **2014**, 14, 112.
- [41] T. P. Padera, B. R. Stoll, J. B. Tooredman, D. Capen, E. di Tomaso, R. K. Jain, *Nature* **2004**, 427, 695.
- [42] S. Kuphal, A. Winklmeier, C. Warnecke, A. K. Bosserhoff, *Eur. J. Cancer* **2010**, 46, 1159.
- [43] M. B. Schaaf, A. D. Garg, P. Agostinis, *Cell Death Dis.* **2018**, 9, 115.
- [44] A. J. Maniotis, R. Folberg, A. Hess, E. A. Seftor, L. M. Gardner, J. Pe'er, J. M. Trent, P. S. Meltzer, M. J. Hendrix, *Am. J. Pathol.* **1999**, 155, 739.
- [45] T. N. Byrne, T. L. Cascino, J. B. Posner, *J. Neuro-Oncol.* **1983**, 1, 313.
- [46] A. Weigand, J. P. Beier, A. Arkudas, M. Al-Abboodi, E. Polykandriotis, R. E. Horch, A. M. Boos, *J. Vis. Exp.* **2016**, 117, 54676.
- [47] A. Grüneboom, I. Hawwari, D. Weidner, S. Culemann, S. Müller, S. Henneberg, A. Brenzel, S. Merz, L. Bornemann, K. Zec, M. Wuelling, L. Kling, M. Hasenberg, S. Voortmann, S. Lang, W. Baum, A. Ohs, O. Kruff, H. H. Quick, M. Jäger, S. Landgraeber, M. Dudda, R. Danuser, J. V. Stein, M. Rohde, K. Gelse, A. I. Garbe, A. Adamczyk, A. M. Westendorf, D. Hoffmann, S. Christiansen, D. R. Engel, A. Vorkamp, G. Krönke, M. Herrmann, T. Kamradt, G. Schett, A. Hasenberg, M. Gunzer, *Nat. Metab.* **2019**, 1, 236.
- [48] A. Thies, U. Mangold, I. Moll, U. Schumacher, *J. Pathol.* **2001**, 195, 537.
- [49] S. Salmi, H. Siiskonen, R. Sironen, K. Tyynele-Korhonen, B. Hirschovits-Gerz, M. Valkonen, P. Auvinen, S. Pasonen-Seppanen, *Melanoma Res.* **2019**, 29, 237.
- [50] A. K. Bosserhoff, M. Golob, R. Buettner, M. Landthaler, R. Hein, *Hautarzt* **1998**, 49, 762.
- [51] O. F. Kuzu, F. D. Nguyen, M. A. Noory, A. Sharma, *Cancer Growth Metastasis* **2015**, 8, 81.
- [52] C. Khanna, K. Hunter, *Carcinogenesis* **2005**, 26, 513.
- [53] W. W. Overwijk, N. P. Restifo, *Current Protocols in Immunology* **2000**, pp. 20.1.1–20.1.29, <https://doi.org/10.1002/0471142735.im2001s39>.
- [54] M. P. Smith, S. Rana, J. Ferguson, E. J. Rowling, K. T. Flaherty, J. A. Wargo, R. Marais, C. Wellbrock, *Pigm. Cell Melanoma Res.* **2019**, 32, 280.
- [55] R. An, R. Schmid, A. Klausung, J. W. Robering, M. Weber, T. Bauerle, R. Detsch, A. R. Boccaccini, R. E. Horch, A. M. Boos, A. Weigand, *FASEB J.* **2018**, 32, 5587.
- [56] A. Klingberg, A. Hasenberg, I. Ludwig-Portugall, A. Medyukhina, L. Männ, A. Brenzel, D. R. Engel, M. T. Figge, C. Kurts, M. Gunzer, *J. Am. Soc. Nephrol.* **2017**, 28, 452.
- [57] D. Schneidereit, S. Nubler, G. Prolss, B. Reischl, S. Schurmann, O. J. Muller, O. Friedrich, *Light: Sci. Appl.* **2018**, 7, 79.
- [58] J. Schindelin, I. Arganda-Carreras, E. Frise, V. Kaynig, M. Longair, T. Pietzsch, S. Preibisch, C. Rueden, S. Saalfeld, B. Schmid, J. Y. Tinevez, D. J. White, V. Hartenstein, K. Eliceiri, P. Tomancak, A. Cardona, *Nat. Methods* **2012**, 9, 676.